ISBN: 978-3-95450-214-1 ISSN: 2673-5490 doi:10.18429/JACoW-IPAC2021-MOPAB059

TOOLS FOR USE OF GENERALIZED GRADIENT EXPANSIONS IN ACCELERATOR SIMULATIONS*

M. Borland, R. Lindberg, R. Soliday, A. Xiao, ANL, Argonne, IL 60439, USA

Abstract

A common assumption in accelerator simulation is that magnets can be approximated using a hard-edge model, perhaps with some edge effects implemented in an impulse approximation. This is usually a good assumption but ignores details of the longitudinal variation of the magnetic fields, which makes it straightforward to implement symplectic tracking. Use of generalized gradient expansions [1, 2] provides an alternative approach that can suppress numerical deficiencies that may be present in computed or measured 3D field maps. However, the computation of the expansions is not particularly straightforward. We describe development of tools that simplify this process and allow use of such expansions in `elegant` [3] . We illustrate using the tools for Advanced Photon Source Upgrade simulations.

INTRODUCTION

The Advanced Photon Source Upgrade [4] uses a hybrid seven-bend achromat lattice [5] with reverse bends [6, 7]. The magnets are strong and short, so z-dependent effects need consideration. The usual approach [8–11] uses hard-edge models with impulsive soft-fringe effects based on fringe-field integrals. These can be compared to direct integration through 3D magnetic fields [12], but this is non-symplectic, does not support long-term tracking studies, and is subject to numerical difficulties. A seldom-used alternative is to employ generalized-gradient expansions (GGEs) [1, 2] to compute the z-dependent vector potential, coupled with a symplectic integrator for particle propagation.

MATHEMATICAL METHODS

Dragt *et al.* [2,13,14] have shown how to express a generic magnetic field as a transverse power series about the nominal orbit. The z-dependent series coefficients are the generalized gradients $C_m(z)$, consisting of "normal" m^{th}-order multipole terms $C_{m,s}(z)$ and skew multipoles $C_{m,c}(z)$. The lowest-order gradients give the on-axis fields $B_x = C_{1,c}(z)$, $B_y = C_{1,s}(z)$, and $B_z = C'_{0,c}(z)$, while off-axis we get contributions from the $C_{m,s}$ and $C_{m,c}$, plus additional contributions that scale with the z-derivative of C. Truncating the sums results in a vector potential that satisfies $\nabla \times B = 0$ to the order of truncation, providing a good series solution to the vacuum Maxwell equations.

The generalized gradients are uniquely determined from magnetic field data on a surface. This approach [2, 13, 14] has smoothing properties within the volume that make it relatively insensitive to noise. Reference [2] showed how to compute the generalized gradients using the normal component of the field on a cylindrical bounding surface, while Refs. [13, 14] present similar formulae for a rectangular boundary. We have found that these algorithms perform well except when computing the gradient $C_0(z)$ that determines the on-axis B_z, but [13, 14] give sufficient hints that we have found workable solutions.

We compute the gradient $C_0(z)$ using the general procedure outlined in Refs. [13, 14], but with a few changes that we outline here. We begin by assuming that we have taken the longitudinal Fourier transform of the magnetic field data on a rectangular cylinder of height h and width w. In our case we wish to find a form of the magnetic field potential that satisfies $\psi(x, y, k) = \tilde{B}_z(x, y, k)/ik$ along the rectangular boundary at $x = \pm w/2$ and $y = \pm h/2$. To facilitate this, we form periodic and odd series of $\tilde{B}_z(x, y; k)$ on each face by reflecting the negative of the data over each endpoint; for example, on the top face we reflect the negative of B_z about the point $x = w/2$ to obtain a periodic and odd function. We then define the Fourier coefficients of the top face as

$$b_n^T(k) = \int_{-w/2}^{w/2} dx \frac{\tilde{B}_z(x, h/2; k)}{w/2} \sin[n\pi(x/w + 1/2)], \quad (1)$$

with a similar definition applying for the bottom face but with $h \to -h$; the right and left faces obtain by swapping $w \leftrightarrow h$ and $x \leftrightarrow y$. By requiring that the normal derivative of the magnetic potential matches B_z on the boundary, we find that $\psi = \psi_T + \psi_B + \psi_R + \psi_L$; the contribution from the top face is

$$\psi_T = \sum_{n=1}^{\infty} \frac{\sinh[(y + h/2)\sqrt{k^2 + (n\pi/w)^2}]}{ik \sinh[h\sqrt{k^2 + (n\pi/w)^2}]} \times b_n^T(k) \sin[n\pi(x/w + 1/2)], \quad (2)$$

while that for the bottom is the same but with $h \to -h$ in the numerator, and the left and right faces obtain by swapping $w \leftrightarrow h$ and $x \leftrightarrow y$.

Finally, we need to convert the potential into a formula for the generalized gradients. This is done by writing the generalized gradient as a sum over the faces

$$C_{m,c} = \sum_{p=0}^{\infty} \left[\mathcal{T}^c_{m,p} b_p^T + \mathcal{B}^c_{m,p} b_p^B + \mathcal{R}^c_{m,p} b_p^R + \mathcal{L}^c_{m,p} b_p^R \right],$$

then inverting the relation between the field and its generalized gradient representation. For the top face, for example,

* Work supported by the U.S. Department of Energy, Office of Science, Office of Basic Energy Sciences, under Contract No. DE-AC02-06CH11357.

ISBN: 978-3-95450-214-1 ISSN: 2673-5490 doi:10.18429/JACoW-IPAC2021-MOPAB059

this involves solving

$$\frac{\sin[n\pi(x/w+1/2)\sinh[(y+h/2)\sqrt{k^2+(n\pi/w)^2}]}{ik2^m m!\sinh[h\sqrt{k^2+(n\pi/w)^2}]} = \sum_{m=0}^{\infty} I_m(kr)\left[\mathcal{T}^c_{m,p}\cos(m\phi)+\mathcal{T}^s_{m,p}\sin(m\phi)\right] \quad (3)$$

for $\mathcal{T}^c_{m,p}$, where (r,ϕ) are polar coordinates in the xy-plane (similar relations apply for the other faces). This is quite involved, but we can extract the $m=0$ component that we need for C_0 by integrating each side over ϕ, obtaining

$$C_{0,c}(k) = \sum_{p=0}^{\infty} \frac{[b_p^T(k)+b_p^B(k)]\sin(p\pi/2)/ik}{2\cosh[\sqrt{k^2+(p\pi/2w)^2}(h/2)]} + \frac{[b_p^L(k)+b_p^R(k)]\sin(p\pi/2)/ik}{2\cosh[\sqrt{k^2+(p\pi/2w)^2}(w/2)]}. \quad (4)$$

We find that while coefficients in (4) diverge as $k \to 0$, the expressions for the derivative $ikC_{0,c}(z) \propto \tilde{B}_z(0,0,k)$ is unambiguous, and gives better results for the on-axis B_z. Hence, while all other gradients require only the normal component of B on the rectangular boundary, if $B_z \neq 0$ on-axis then one will also need to know B_z on the surface.

TOOLS

Since 2016, `elegant` had the ability to propagate particles through GGEs using a sympletic integrator. This was recently improved to include skew fields. Two companion programs were recently written to perform GGEs for use in `elegant`: `computeCBGGE`, accepts data on a circular cylinder, while `computeRBGGE` accepts data on four bounding planes. The latter does not cover dipoles that require use of a "bent" boundary, but covers wigglers and moderate-angle dipoles. The user either provides (z,ϕ,B_ρ) data in an SDDS file [15] or (z,x,y,B_x,B_y,B_z) data in a set of four SDDS files, one for each plane of the rectangular cylinder.

With perfect data and numerical precision, using more derivatives and multipoles would give better agreement between the data and expansion-generated fields. In practice, adding too many derivatives and multipoles makes agreement worse. To lessen the burden of finding the best expansion, both programs will auto-tune the number of derivatives and multipoles to best match the user-provided data.

SEPTUM LEAKAGE FIELD

An important motivation for developing `computeRBGGE` was evaluation of the Lambertson septum [16] for the APS-U vertical-plane injection scheme [17]. Since the design uses cancellation of large fields between different parts of the magnet to achieve low leakage field, an error could significantly impact the nonlinear dynamics [18]. Numerical integration through gridded 3D fields is not symplectic, and thus is unsuitable for long-term tracking, motivating use of GGEs with measured field data. As Fig. 1 shows, the on-axis GGE does not precisely reproduce the measured fields, which may be an issue with magnetic measurements. The rms error is less than 0.55 mT over the entire field map.

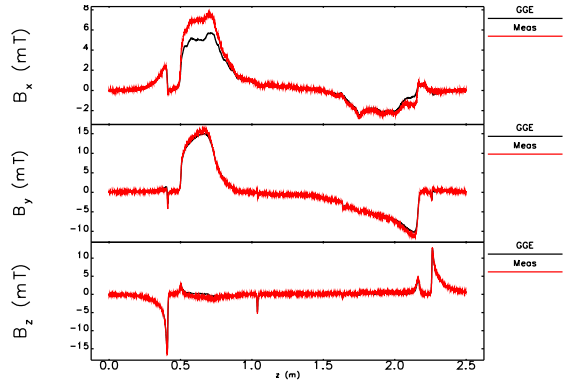

Figure 1: On-axis fields from APS-U Lambertson septum prototype from measurements and GGE.

We used the GGE to model the septum in APS-U using `Pelegant` [19] for 100 post-commissioning configurations [20]. As Fig. 2 shows, the effect on the dynamic acceptance is modest even if the leakage fields are doubled from the measured result. In addition, the median Touschek lifetime is reduced by only about 1%, showing that the as-built septum is acceptable magnetically.

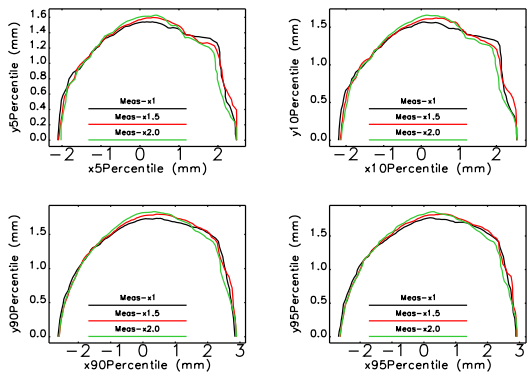

Figure 2: Dynamic acceptance of APS-U with Lambertson leakage field from generalized gradient expansion based on measurements. x1.5 and x2.0 show results with leakage multiplied by the indicated factors.

APS-U LATTICE

Another goal in using GGEs is more accurate modeling of APS-U main magnets. We used data from 3D magnetic models, taking rectangular-boundary data for dipoles and cylindrical-boundary data for straight multipoles. In choosing the rectangular boundaries, care was taken to encompass the curved beam path while avoiding iron poles. Table 1 shows the parameters needed to get the best agreement between the GGE and the 3D field data.

Since the magnetic models do not correspond precisely to the working strength of each magnet, we scaled each GGE to match the first-order (second-order) transport matrix for each

ISBN: 978-3-95450-214-1 ISSN: 2673-5490 doi:10.18429/JACoW-IPAC2021-MOPAB059

Table 1: Optimal Parameters for GGEs of APS-U Magnets

Magnet	Type	m	d	frac. rms error
M1, M2	LGD	7	1, 2	1×10^{-2}, 6×10^{-3}
M3, M4	NTGD	3	2	7×10^{-3}, 4×10^{-3}
Q1, Q2	Quad	10	5, 6	5×10^{-4}
Q3/Q6, Q7	Quad	10	6, 5	4×10^{-4}
Q4	RTGD	8	4	6×10^{-4}
Q5	RTGD	3	3	8×10^{-4}
Q8	RTGD	10	3	3×10^{-4}
S1/S3, S2	Sext	9	7	4×10^{-4}, 3×10^{-4}

dipole and quadrupole (sextupole), using the standard lattice elemments as the target. This was facilitated by `elegant`'s ability to compute transfer matrices for any system using parallel particle tracking [21]. For dipoles, we simultaneously allow the magnet to move horizontally and longitudinally in order to null out any angle or position offsets. Typically matrix elements (in SI units) are matched within 10^{-3} to 3×10^{-5}, with better values for quadrupoles and sextupoles. The strongest of the reverse-direction transverse-gradient dipoles, the Q8 family, showed the worst agreement, at the 9×10^{-3} level.

Having tuned each GGE individually, we replaced ordinary lattice elements with GGEs, allowing comparison, e.g., to the full-lattice tunes of $\nu_x = 95.1$ and $\nu_y = 36.1$. Replacing only quadrupoles and sextupoles confirmed the basic process, giving $\nu_x = 95.093$ and $\nu_y = 36.084$ and whole-ring chromaticity errors of $\xi_x = 0.055$ and $\xi_y = 0.074$. Additionally replacing normal-bending transverse-gradient dipoles (NTGDs) with GGEs gave $\nu_x = 95.100$ and $\nu_y = 36.113$. Additionally replacing reverse-bending transverse-gradient dipoles (RTGDs) gave $\nu_x = 94.871$ and $\nu_y = 35.959$ (these are horizontally-focusing magnets). Finally, additionally replacing the two families of longitudinal-gradient dipoles (LGDs) with GGEs gave $\nu_x = 94.876$ and $\nu_y = 35.870$.

The changes from the LGDs are similar to effects seen when tracking directly with 3D field maps and are attributed to nominally-cancelling edge and body sextupole terms in the straight magnets, which produce local gradients due to the curved trajectory. The changes from the RTGDs were surprising, particularly since the NTGDs are considerably stronger. However, the RTGDs are relatively short and soft edge effects are not included in the model, pointing to the need to improve edge modeling in short TGDs.

We next used `elegant`'s optimizer to adjust the GGE parameters to restore the tunes and lattice functions, emulating the real-world process of adapting magnet settings to magnetic measurement results, as well as lattice correction. With this in hand, we performed various tracking studies. For example, Fig. 3 compares the momentum tune dependence for the design and GGE models, showing fairly good agreement. The chromaticities from the GGE model are $\xi_x = 8.12$ and $\xi_y = 4.74$; fits to GGE tracking give similar values of $\xi_x = 8.07$ and $\xi_y = 4.73$.

Figure 4 shows that frequency map analysis [22] for the conventional and GGE models agrees well, with the GGE-based model showing slightly higher tune shift with vertical

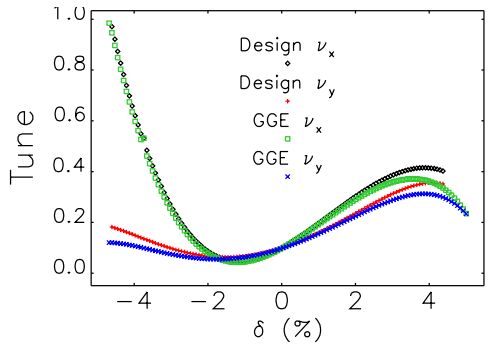

Figure 3: Comparison of momentum detuning for design and GGE models.

amplitude. The GGE-based run took about 180 times as

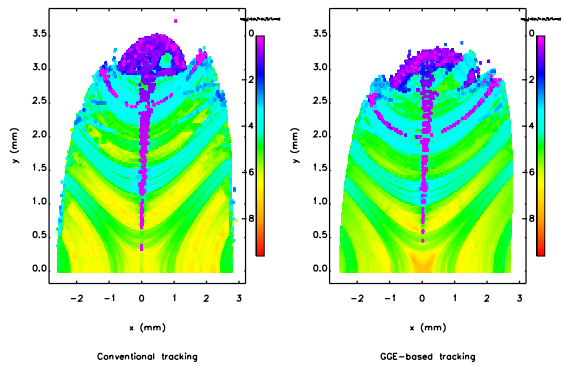

Figure 4: Comparison of FMA for APS-U.

long. Although this is not prohibitive for a parallel code, it emphasizes that GGE methods are best used sparingly or to provide reference data for assessing other methods.

CONCLUSIONS

We developed convenient tools allowing creation of generalized gradient expansions for straight multipole magnets and small-angle dipole magnets. These tools are distributed with `elegant` and interface to it using SDDS files. We used these tools to evaluate the Lambertson septum for APS-U starting from measured 3D field fields. We also developed a full model of the APS-U storage ring using only generalized gradient expansions and drifts. This appears to be a first, as previous efforts have involved only single elements inserted into a lattice [23, 24]. (See, however, [25] for similar work using another method.) Preliminary exploration of beam dynamics using this model shows good agreement with conventional modeling.

ACKNOWLEDGMENTS

Thanks to M. Jaski for field data for APS-U designs, M. Kasa for Lambertson measured data, and M. Venturini and C. Mitchell for references. Simulations used the Bebop cluster at Argonnne's LCRC.

ISBN: 978-3-95450-214-1 ISSN: 2673-5490 doi:10.18429/JACoW-IPAC2021-MOPAB059

REFERENCES

[1] M. Venturini, "Lie Methods, Exact Map Computation, and the Problem of Dispersion in Space Charge Dominated Beams", Ph.D. thesis, University of Maryland, Maryland, USA, 1998.

[2] M. Venturini and A. Dragt, "Accurate computation of transfer maps from magnetic field data", *NIM A*, vol. 427, pp. 387–392, May 1999. doi:10.1016/S0168-9002(98)01518-6

[3] M. Borland, "elegant: A Flexible SDDS-Compliant Code for Accelerator Simulation", Advanced Photon Source, Tech. Rep. ANL/APS LS-287, Sep. 2000.

[4] M. Borland *et al.*, "The Upgrade of the Advanced Photon Source", in *Proc. IPAC'18*, Vancouver, Canada, Apr.-May 2018, pp. 2872–2877. doi:10.18429/JACoW-IPAC2018-THXGBD1

[5] L. Farvacque *et al.*, "A Low-emittance Lattice for the ESRF", in *Proc. IPAC'13*, Shanghai, China, May 2013, paper MOPEA008, pp. 79-81.

[6] J. Delahaye and J. P. Potier, "Reverse bending magnets in a combined-function lattice for the CLIC damping ring", in *Proc. PAC'89*, pp. 1611–1613, 1990. doi:10.1109/pac.1989.72869

[7] A. Streun, "The anti-bend cell for ultralow emittance storage ring lattices", *NIM A*, vol. 737, pp. 148–154, Feb. 2014. doi:10.1016/j.nima.2013.11.064

[8] K. L. Brown, "A First- and Second-Order Matrix Theory for the Design of Beam Transport Systems and Charged Particle Spectrometers", Stanford Linear Accelerator Center, CA, USA, Tech. Rep. SLAC-R-75, Jan. 1967. doi:10.2172/4496097

[9] G. E. Lee-Whiting, "End effects in first-order theory of quadrupole lenses", *NIM A*, vol. 76, no. 2, pp. 305–316, Dec. 1969. doi:10.1016/0029-554x(69)90033-0

[10] J. Irwin and C.-X. Wang, "Explicit soft fringe maps of a quadrupole", in *Proc. PAC'95*, pp. 2376–2378, 1996. doi:10.1109/pac.1995.505558

[11] D. Zhou, J. Y. Tang, Y. Chen, and N. Wang, "Explicit maps for the fringe field of a quadrupole", in *Proc. IPAC'10*, Kyoto, Japan, May 2010, paper THPD091, pp. 4500–4502.

[12] M. Borland *et al.*, "Modeling of dipole and quadrupole fringe-field effects for the Advanced Photon Source Upgrade lattice", in *Proc. NAPAC'16*, Chicago, IL, USA, Oct. 2016, pp. 1119–1122. doi:10.18429/JACoW-NAPAC2016-THPOA13

[13] A. J. Dragt, *Lie Methods for Nonlinear Dynamics with Applications to Accelerator Physics*. Maryland, USA: University of Maryland, 2009.

[14] C. Mitchell, "Calculation of Realistic Charged-Particle Transfer Maps", Ph.D. thesis, University of Maryland, Maryland, USA, 2007.

[15] M. Borland, "A self-describing file protocol for simulation integration and shared postprocessors", in *Proc. PAC'95* , Dallas, TX, USA, May 1995, paper WAE11, pp. 2184–2186.

[16] M. Abliz *et al.*, "A concept for canceling the leakage field inside the stored beam chamber of a septum magnet", *NIM A*, vol. 886, pp. 7–12, 2018. doi:10.1016/j.nima.2017.11.090

[17] A. Xiao, M. Borland, and C. Yao, "On-axis Injection Scheme for Ultra-Low-Emittance Light Sources", in *Proc. NAPAC'13*, Pasadena, CA, USA, Sep.-Oct. 2013, paper WEPSM13, pp. 1076–1078.

[18] A. Xiao, M. Borland, and M. Abliz, "Simulation study with Septum field map for the APS upgrade", in *Proc. NAPAC'19*, Lansing, MI, USA, Sep. 2019, paper MOPLM10, pp. 116-119.

[19] Y. Wang and M. Borland, "Pelegant: A Parallel Accelerator Simulation Code for Electron Generation and Tracking", *AIP Conf. Proc.*, vol. 877, p. 241, 2006. doi:10.1063/1.2409141

[20] V. Sajaev, "Commissioning simulations for the aps upgrade lattice", *Phys. Rev. Accel. Beams*, vol. 22, p. 040102, 2019. doi:10.1103/physrevaccelbeams.22.040102

[21] M. Borland, "A High-Brightness Thermionic Microwave Electron Gun", Ph.D. thesis, Stanford University, Stanford, USA, 1991.

[22] J. Laskar and D. M. Robin, "Application of frequency map analysis to the als", *Part. Accel.*, vol. 54, pp. 183–192, 1996. http://cds.cern.ch/record/301630

[23] M. Venturini, "Effect of Wiggler insertions on the single-particle dynamics of the NLC main damping rings", LBNL, Berkeley, CA, USA, Tech. Rep. LBNL-53264, 2003.

[24] A. Wolski *et al.*, "Frequency map analysis of nonlinear dynamics in the NLC main damping rings", LBNL, Berkeley, CA, USA, Tech. Rep. LBNL-56505, 2004.

[25] L. Bojtar, "Frequency analysis and dynamic aperture studies in a low energy antiproton ring with realistic 3D magnetic fields", *Phys. Rev. Accel. Beams*, vol. 23, p. 104002, 2020. doi:10.1103/physrevaccelbeams.23.104002